

Basin shear wave velocities beneath Seattle, Washington from noise-correlation

Rayleigh waves

Andrew A. Delorey (Corresponding Author)

John E. Vidale

Department of Earth and Space Sciences

University of Washington

Johnson Hall Rm-070, Box 351310

4000 15th Avenue NE

Seattle, WA 98195-1310

Three figures are included as electronic supplements to this manuscript that show vertical cross-sections of our new shear wave velocity model for the Seattle Basin and a comparison between our model and that of Snelson *et al.*, (2007).

ABSTRACT

We produced a new S-wave velocity model for the Seattle Basin using direct observations rather than by using a P-wave velocity model and a V_p/V_s ratio as all previous full basin models have been constructed. Our results reveal greater detail in the upper 3.5 km than previous models. Simulations calculated using our new model better predict peak ground velocities (PGV) at periods between 1-2s for two local earthquakes than the previous model used to calculate Seattle's seismic hazard map.

Tomography with short-period Rayleigh waves, extracted using noise interferometry, can refine S-wave velocity models in urban areas with dense arrays of short-period and broadband instruments. We apply this technique to the Seattle area to develop a new shallow S-wave model for use in hazard assessment. Continuous data from the Seismic Hazards in Puget Sound (SHIPS) array and local broadband stations have inter-station distances of 90 km or less. This spacing allows us to extract Rayleigh waves between 2-10s period that are sensitive to shallow basin structure.

We collected data from two local earthquakes and run finite-difference simulations using our new velocity model as well as the previous velocity model used in development of the Seattle seismic hazard maps to assess how well our model predicts ground motions relative to the previous model. With a recent deployment of Netquakes strong motion stations by the Pacific Northwest Seismic Network (PNSN) and the U.S. Geological Survey we are now able to make more comprehensive assessments of the predictions for recent events.

INTRODUCTION

Seattle, Washington, one of the biggest cities in the United States that is threatened by earthquakes, sits atop a deep sedimentary basin. Nearby, Everett and Tacoma, Washington have a similar setting (Figure 1). These basin structures are the result of the evolution of the Puget Lowland fore arc basin, which combines strike-slip and thrust-fault earthquakes to accommodate right-lateral strike-slip and N-S shortening (Johnson *et al.*, 1996; Pratt *et al.*, 1997). The N-S shortening is driven by the oblique subduction of the Juan de Fuca plate under the North American plate (Riddihough, 1984). As a result, Cascadia is being squeezed between the Sierra Nevada block and western Canada (Wells *et al.*, 1998; Wells and Simpson, 2001).

The Seattle Basin is described in a number of papers (Blakely *et al.*, 2002; Brocher *et al.*, 2001; Pratt *et al.*, 1997; ten Brink *et al.*, 2002; ten Brink *et al.*, 2006). The nearby Tacoma Basin (Brocher *et al.*, 2001; Pratt *et al.*, 1997) and Everett Basin (Johnson *et al.*, 1996) have also been studied, but remain less well understood. The Kingston Arch separates the Seattle Basin from the Everett Basin, and the Seattle Uplift separates the Seattle Basin from the Tacoma Basin. In a series of studies, models were developed for these basins because the basins are known to amplify seismic shaking and many of the their buildings were constructed before knowledge of the severity of earthquake hazards (Barberopoulou *et al.*, 2004; Brocher *et al.*, 2004; Frankel *et al.*, 1999; Frankel *et al.*, 2002; Pratt *et al.*, 2003a).

The basins of the Puget Lowland require study to improve modeling of three-dimensional features. The young unconsolidated deposits are a temporally and spatially complex stratigraphy of glacial outwash, till, lacustrine, and recessional deposits formed

when the Lowland was glaciated at least six different times in the Pleistocene (Booth, 1994). The top several kilometers are peppered with smaller-scale basins and the deeper basins are likely delineated by the major bounding faults.

SEISMIC HAZARDS

Three types of earthquakes periodically occur in the Seattle area, as is typical for subduction zones:

(1) Most damaging for the urbanized areas are the shallow crustal events (Haugerud *et al.*, 2003; Sherrod *et al.*, 2004; ten Brink *et al.*, 2002) due in part to their close proximity. The most recent documented instance of a large event on the Seattle fault was the M7.2 event in about 900AD (ten Brink *et al.*, 2006), which featured 7m of surface slip. There is also evidence of uplift in the vicinity of the Tacoma Fault about 1000 years ago (Brocher *et al.*, 2001). Numerous other faults are present, and more are being found as geologists image the landscape with Light Detection And Ranging (LIDAR), but which faults are currently active and their recurrence intervals are not well known.

(2) M9 events strike the Cascadia coast roughly every 500 years (Atwater, 1992; Goldfinger *et al.*, 2003; Satake *et al.*, 2003). These events produce strong long-period basin excitation lasting many minutes.

(3) Deep earthquakes within the subducting slab has been the most common cause of strong earthquakes in recent decades, with M6.5 to M7 events in 1949, 1965, and 2001.

Seismic hazards are commonly estimated by predicting the shaking at a hard rock site from vertically incident seismic waves using a regional velocity model, then applying an amplification factor for non-hard rock sites that account for the effects of loose, unconsolidated sediments. However, the basins have an additional effect of focusing and

trapping energy within them (Frankel *et al.*, 2002; Frankel *et al.*, 2007), which is not modeled with many traditional methods.

Some of the patterns of shaking have been captured with studies solely examining site amplification (Hartzell *et al.*, 2000). Those results, however, are difficult to extrapolate to the sites for which recordings have not been analyzed, and to the many sites for which back-azimuth to an earthquake has a strong influence on the motions. Recorded ground motions from both strong and weak shaking indicate patterns of amplification that vary with site location, source location, and frequency (Barberopoulou *et al.*, 2004; Frankel *et al.*, 2002).

PREVIOUS MODELS

Earthquake tomography and active-source experiments have revealed the larger-scale features of the crust around Seattle (Lees and Crosson, 1990; Pitarka *et al.*, 2004; Pratt *et al.*, 1997; Symons and Crosson, 1997; Van Wagoner *et al.*, 2002) as well as northern Cascadia (Ramachandran *et al.*, 2004; Ramachandran *et al.*, 2005; Ramachandran *et al.*, 2006). Tomographic models indicate a Seattle Basin structure that has a symmetrical bowl shape in the E-W direction and asymmetry in the N-S direction consistent with formation by motion of the Seattle Fault. These studies find a crustal thickness of 35 km (Schultz and Crosson, 1996), and provide a useful regional velocity model as a starting point for basin models, but do not have adequate resolution to model basin waves. Also, because they were mostly derived from short-period, vertical-component seismometers, S-waves are difficult to reliably identify, and thus S-wave models are less well constrained.

High-resolution basin models have been solely built on P-wave observations until the most recent work (Snelson *et al.*, 2007), but this model is only a two-dimensional cross-section. The larger-scale S-wave velocity models are derived from the conversion of a P-wave velocity model through an assumed Poisson's ratio. Fluid content, porosity, and composition all affect Poisson's ratio, so a direct measurement of S-wave velocities is preferable. For velocities appropriate for sedimentary basins, data used to determine Brocher's (2005) empirical relationship between V_p and V_s are highly scattered. To the first order, his relationship is a good approximation, but the V_p/V_s ratio is not simply a function of V_p for sedimentary rocks.

Important details remain unresolved (Snelson *et al.*, 2007). The thickness of the unconsolidated layers in recent models varies by up to a factor of two, which needs resolution. The inference of several shallow sub-basins would benefit from verification and further study. Attenuation, a critical parameter for estimates of ground shaking, has only been estimated from active source experiments (Li *et al.*, 2006). Several different hypotheses exist for why the largest amplification peaks occur at stations above the deepest part of the Seattle Basin, such as focusing of teleseismic energy by the serpentinized upper mantle, or that the observed amplification is primarily controlled by unconsolidated sediments (Pratt *et al.*, 2003a).

MODEL CALCULATION

We calculated the 3-D shear wave velocity model in two steps. In the first step, we solved for the 2-D Rayleigh wave phase velocity model as a function of period between 2 and 10 seconds. The model space is 110 km east to west and 145 km north to south, centered on Seattle. The velocity model was parameterized with an irregularly spaced grid, with smaller spacing in regions with greater data coverage. Inter-grid spacing ranged from 1 km near central Seattle to 20 km at the edges of the model. At each grid point, we used a 3rd order polynomial for phase velocity as a function of frequency. At each frequency and grid point, we calculated a Gaussian surface with a characteristic width equal to the square of the distance to the next closest grid point. The normalized sum of these surfaces determined the 2-D velocity model at each frequency. We used a starting model that was a 1D average of the Stephenson (2007) model and two different forward calculations, ray theory and a single-scatterer approximation, to calculate the polynomial coefficients.

We inverted for the polynomial coefficients of the model using the following equation:

$$\underline{m} = \left(\underline{G}^T \underline{C}^{-1} \underline{G} + \gamma^2 \underline{L}^T \underline{L} \right)^{-1} \underline{G}^T \underline{C}^{-1} \underline{d}$$

\underline{C} is the data covariance matrix. \underline{G} is the partial derivative matrix. \underline{L} is the normalization matrix described below. γ is a scaling parameter between goodness of fit and the normalization matrix. \underline{d} is the data vector of observed phase velocities and \underline{m} is the model vector of polynomial coefficients.

In determining the data uncertainties for matrix \underline{C} we estimated the uncertainties in calculating the Rayleigh wave phase velocities. The most important source of error in

our phase velocity calculation was the way we augmented our dataset and solved the phase ambiguity using the model of Stephenson (2007). To test the error that would be introduced if our assumption that the phase velocity is 3.91 km/s at 20 seconds everywhere in the model were incorrect, we considered other values. If we were off the actual phase velocity by 5% at a period of 20 seconds, the error introduced would only be about 2% at a period of 2 seconds, less for periods between 2 and 10 seconds. Another source of error comes from the possibility of phase shifting in the empirical Green's functions if the azimuthal distribution of coherent noise at the periods we used was highly focused, though we did not find that to be the case. It was difficult to know for sure how much error is present, so we used a conservative estimate of 10% in our inversion.

The normalization matrix (L) is the sum of two different matrices. The first matrix is a diagonal matrix whose values were determined by the geographic location of the corresponding parameter. For each grid point, we calculated its mean distance to all of the stations, which is used as a proxy for the relative amount of data coverage. For points with a low mean distance we gave a lower variance and for stations with a high mean distance we give a higher variance. In this way we were able to discourage parts of the model with sparse data coverage from drifting very far from the starting model and simultaneously emphasize perturbations calculated for the parts of the model with a high density of observations. The second matrix measured the geographic roughness in the model using a finite difference approximation of the curvature. With this matrix we were able to apply a penalty for increasing roughness.

In order to estimate the effect of the starting model on our results, we ran this inversion using many different starting models. Beginning with our basic starting model,

we added Gaussian noise with a standard deviation of 20% to all model nodes within the basin. We ran each of these models to a solution then calculated the mean and standard deviation of the results. Within the basin, most regions showed a standard deviation of much less than 10%, with a few isolated spots as high as 15% where data coverage was sparse. This indicated that there is some dependence on the starting model mostly in the shallowest layers, but the variations were within our estimated uncertainties.

In the second step, we inverted the Rayleigh wave dispersion curves for the 3-D isotropic shear wave velocity structure. The horizontal dimensions are 60x60 km, centered on Seattle with uniform horizontal grid spacing of 2.5 km. The phase velocity model was bigger than the shear wave velocity model in order to include several stations outside the basin. However, for the shear wave velocity inversion, it was no longer necessary that those stations lie within the model so we omitted parts of the model with the poorest data coverage. The vertical extent of the model was 160 km in depth in order to avoid any boundary problems with the forward problem, however the Rayleigh wave frequencies we estimate were most sensitive to the top ~4 km of the model. Between 4 and 9 km depths, velocities were highly smoothed in part because we assigned higher penalties for roughness and deviation from the starting model at these depths and below. The grid spacing in the upper 10 km of the model ranged from 0.25 km to 1 km and the spacing size increases with depth through the rest of the model. We considered inclusion of a water layer for Puget Sound and Lake Washington, but at periods of 2 seconds and greater, the effect of the water layer for the relevant depths was only about 1 percent and only in very localized places.

We used a starting model based on Stephenson (2007) and calculated synthetic dispersions curves in our forward calculation using the method of Takeuchi and Saito [1972]. We used a full 3-D inversion so that we could apply normalization to the model as a whole. Our shear wave velocity inversion was similar to our phase velocity inversion described above. We used two normalization matrices: one was a Laplacian matrix that is designed to apply a penalty for increasing roughness, and the other was a parameter variance matrix that allows us to hold steady model parameters that were in regions not well constrained by the data while allowing other parameters to vary more freely. In particular, we assigned high variances to parameters deeper than 9 km since that is below the bottom of the Seattle Basin, where we had little constraints from our data. As in the first inversion, we calculated solutions from a number of starting models perturbed by adding Gaussian noise to our original starting model. This time, the standard deviation of the noise was 5% and the same noise is added to all points in a column. We used smaller levels of noise than with our phase velocity calculations because adding higher levels of noise could have led to the generation of physically unrealistic velocity structures, which caused problems with the forward calculations. The resulting suite of models has a standard deviation of only about one percent except in the uppermost layer.

DATA

Most of our data came from the Seattle SHIPS array (Pratt *et al.*, 2003b) with some additional data from stations around Seattle from the Pacific Northwest Seismic Network (PNSN) and Earthscope's Transportable Array (TA) (Figure 2). During the Seattle SHIPS experiment, seismometers were deployed at 87 sites in a 110-km-long east-west line, three north-south lines, and a grid throughout the Seattle urban area from January to May 2002. Each site recorded three-components of velocity using a 2-Hz L-22 sensor recording 50 samples per second. The PNSN and TA sites had three-component broadband Streckeisen STS-2, Guralp CMG-40T, or Guralp CMG-3T sensors recording 40 samples per second.

The L-22 sensor is a short-period instrument. However, we were able to determine Rayleigh wave group velocities out to periods 10 seconds or more in some cases by careful selection and processing of the data. Each instrument was individually calibrated during the SHIPS experiment and we used the individual calibrations to deconvolve the instrument response, eliminating most of the variability in response among the instruments. According to the calibrations, the velocity sensitivity was on the order of 100 times higher at a period of one second than at a period of 10 seconds. Still, the amplitude of coherent energy at a period of 10 seconds was often high enough to observe a good Rayleigh wave signal. We whitened the spectrum before bandpass filtering to ensure the proper frequency content in each wavelet despite frequency-dependent instrument sensitivity.

To extract Rayleigh wave wavelets, the vertical-component seismograms from all stations were merged then cut to daylong segments. The instrument response was

deconvolved, the signal was integrated to displacement, and the data down-sampled to 10 samples per second. The cross-correlations were computed as in Bensen *et al.*, (2007). We used one-bit amplitude normalization because it produced cleaner and more prominent Rayleigh wave wavelets than other amplitude normalization methods. Many station pairs were discarded if the station distance was not sufficiently large relative to the wavelength of the surface wave. Though we did not use a specific distance cut-off, we used only well-formed surface wave wavelets. We used an automated system to discard the worst traces and manually evaluated the rest. Due to our selectivity in picking only the best data, we used only 13% of the possible paths. Two examples of bandpassed empirical Green's functions are shown in Figure 3. In these two examples, noise coherence is very good from 10 seconds down to 2-3 seconds.

We first calculated the group velocity dispersion curve of each trace, starting at the longest period available, by calculating and selecting the peak of the envelope function. Traces that did not have coherence to at least 10 seconds period were discarded. When we could not obtain the group velocity dispersion up to a period of 20 seconds, which occurred in most of our paths, we extrapolated the curve by using group velocity measurements calculated from the velocity model of Stephenson (2007). By applying a bandpass filter in small increments to our waveforms, we were able to track the peak of the envelope function to shorter periods, often down to between 2 and 3 seconds. We terminated our group velocity curve when the signal-to-noise ratio fell below 11.5 dB, or if the peak of the envelope function jumped, split, or was otherwise ambiguous to track. The evaluation criteria were defined to select the most promising

dispersion curves, which we then evaluated visually. The paths used are shown in Figure 4.

As described in Bensen *et al.*, (2007), an additional constraint was needed to resolve the phase ambiguity associated with the calculation of surface wave phase velocities from group velocities. To solve this ambiguity we calculated Rayleigh wave phase velocity dispersion curves for a uniform grid of 1-D profiles taken from the shear wave velocity model of Stephenson (2007), using the method of Takeuchi and Saito (1972). Throughout the model, the calculated phase velocity dispersion curves converge to ~3.91 km/s at a period of 20 seconds indicating a nearly 1-D velocity structure beneath the Seattle Basin, i.e. depths below 9km. Calculated phase velocities ranged from 1 to 2.25 km/s at a period of 1 second indicating that velocities at basin depths vary laterally. We assumed that the Rayleigh wave phase velocity is 3.91 km/s at a period of 20 seconds everywhere beneath the Seattle Basin and integrated the group velocity curve from 20 seconds down to 2 seconds to determine phase velocities at these shorter periods. The group velocity curve between 20 and 10 seconds was based on a combination of values from the model of Stephenson (2007) and from our cross-correlations. The group velocity curve between 10 and 2 seconds was based exclusively on our cross-correlations. In this fashion, we resolved the phase ambiguity and calculated the phase velocity dispersion curve from the group velocity dispersion curve using the phase velocity at a period of 20 seconds as the constant of integration:

$$S_c(\omega) = \omega^{-1} \left(\int_{\omega_n}^{\omega} s_u(\omega) d\omega + \omega_n s_c^n \right),$$

in which s_u is the group slowness, s_c is the phase slowness and the “n” indicates a period of 20 seconds (Bensen *et al.*, 2007).

The SHIPS array was not designed for this kind of analysis and the station layout is not ideal for surface wave tomography. In order for velocities to be well resolved for a model parameter, there must be several or many independent observations of the region in the form of crossing ray paths. For most of the periods we used, there are many crossing ray paths near the center of the model corresponding to the city of Seattle. Away from the center of the model there are fewer crossing paths and at its perimeter, there are almost none. The lack of crossing ray paths can lead to the smearing of velocity perturbations along a ray's path.

We performed a resolution test to examine the horizontal resolution of our dataset (Figure 5). In this test we started with a 1D model, then generated a checkerboard pattern of higher and lower velocities with width of 4 km and a perturbation magnitude of 5-10% from the 1D model. Due to our irregularly spaced grid, not every velocity perturbation has exactly the same magnitude. We generated synthetic data from this perturbed 1D model, then ran our inversion using the 1D model as a starting model. The misfit reduction after three iterations of our inversion is 98%. Our recovery of the synthetic model was very good at periods of 3 seconds and above, and not very good at 2 seconds due to the limited number of paths used at this period. Vertical resolution is a little bit more difficult to assess because it depends upon the frequency range of the Rayleigh waves as well as path coverage. We do not, however, have the ability to resolve a feature as small as the potential velocity reversal beneath the hanging wall of the Seattle fault regardless of which fault model is assumed.

RESULTS

Our Rayleigh wave phase velocity results show a clear low velocity zone that is consistent with the area of low residual isostatic residual gravity shown in Figure 1, measuring ~60 km from east to west and ~45 km from north to south (Figure 6). The lowest velocities at all periods are near downtown Seattle, just to the north of the Seattle fault. Rayleigh waves with periods between 2 and 6 seconds are sensitive to the upper 5 km in this setting and those with periods between 8 and 10 seconds are sensitive to the depth range 5-15 km. At a period of 2 seconds the velocities are as low as ~625 km/s, and the lowest velocities at a period of 10 seconds are 960 km/s. With increasing period, the apparent diameter of the basin shrinks. Potential sub-basins are revealed in the southwest, north, and east. There is less apparent structure in the deeper parts of the basin. However, due to the broadening sensitivity kernels of Rayleigh waves at longer periods, it is also more difficult to resolve smaller structures with 8 to 10 second waves.

Our shear wave velocity results show that velocities are slower in some areas in the top 1.5 km of the Seattle Basin beneath the city of Seattle than in the model of Stephenson (2007) (Figure 7). Additional images of our model are included as an electronic supplement. Our dataset does not uniquely constrain the uppermost ~250 m of the basin, but by using a 1-D average from the model of Stephenson (2007) as our starting model, we inherit the ~600 km/s velocities in the uppermost layers from that model. By using different plausible starting models, the uppermost layer could be anywhere from 400-750 m/s according to our calculations. At 500m and below, our calculations show little dependence on the starting model. Beneath the uppermost layers we found low velocities persist to at least 3 km, where our velocities were lowest just

north of the Seattle Fault with lesser amounts in other parts of the basin. Below 3 km our results show velocities approaching those of Stephenson (2007).

We compared the 2-D refraction profile of Snelson *et al.*, (2007), that runs west to east across the Seattle Basin, to the same region from our new model. The Snelson *et al.*, (2007) model has an origin at sea level and includes topography while the origin of our model is the ground surface and does not include topography. If we align the top of the two models disregarding the two different depth axes and look at the top 4 km where the models overlap we can compare velocity contours. The biggest difference between the two models is that our model is a little slower in the top 1 km. To the west of Puget Sound our model is slower throughout the top 4km. Between Puget Sound and Lake Washington our model is a faster in the 1-3 km range then two models are very similar below 3 km. To the east of Lake Washington our model is generally faster below 1 km. The Snelson *et al.*, (2007) model is missing contours beneath Puget Sound and Lake Washington due to a lack of ray paths so we cannot compare these regions. A comparison of the two sets of contours is included as an electronic supplement.

MODEL VALIDATION

We assessed our new model's ability to predict amplitudes in the 1-2 second range relative the model of Stephenson (2007) because it was used in the development of Seattle's seismic hazard maps and because it was validated in this period range . There are other models we could use for comparison. However some of them were not tested at the shorter periods we address here e.g. (Pitarka *et al.*, 2004), while others are not well constrained in the shallowest parts of the basin (1.0-3.5 km) where our model is well constrained, e.g. (Van Wagoner *et al.*, 2002), or not 3D, e.g. (Snelson *et al.*, 2007). Also, since other 3D shear wave velocity models are dependent on an accurate Vp/Vs ratio, and Vp/Vs ratios are highly variable for sedimentary rocks (Brocher, 2005), it would be hard to know if any differences between models are due to the tomography or due to the Vp/Vs ratio. So while the Stephenson (2007) model is not necessarily the best overall model at the time of this report, it is the most relevant comparison in addressing our motives for improving seismic hazard assessments and the other models do not offer a straight-forward validation.

For all of our amplitude comparisons we calculated waveform envelopes. We calculated peak velocity in a window that starts just before the direct shear wave arrival and ends after the direct surface wave arrival, and then we took the geometric mean of the two horizontal components to capture both Love and Rayleigh waves. We used periods between 1-2 seconds because this is the band in which many smaller buildings and transportation infrastructure are vulnerable and because in this band is where we expected the most differences between the two models.

Frankel (2009) showed a good phase match between data and synthetics for the 2001 Nisqually 6.8 event in the 0.2-0.4 Hz band using the Stephenson (2007) model. We expected and produced very similar results in this band using our local model embedded in the Stephenson (2007) regional model because waves in this band are not strongly affected by our updates to shallow structure from our tomography results. At shorter periods addressed in this study, we neither expected nor achieved a good phase match between synthetics and data. We based our validation on the arrivals and velocity amplitudes of the shear and surface waves.

In Figure 8 we show a data and synthetic to demonstrate what we considered a well-fitting prediction. Many of the urban strong motion sensors used in this study are by necessity located in noisy locations. Even though there is some noise in the data, the shear wave and surface wave arrivals on the horizontal components are very close in arrival time and amplitude despite a phase mismatch. On the north component, the synthetic shear wave has a higher amplitude than the data, but on the east component that relationship is reversed. These differences could be the result of an issue with the modeled radiation pattern or unmodeled anisotropy, as well as small inaccuracies in velocity model. Since we use the mean of both horizontal components and because the well-fitting surface wave controls the maximum amplitude in this example, it yields an excellent match. In addition, the amplitude of the coda is similar throughout this fifty-second trace even though we didn't consider the coda in our evaluation. In some other examples one of the horizontal components fits well while the other one does not, or the arrival times are shifted slightly. Unmodeled scattering, focusing and/or multipathing could explain some of these amplitude, phase, or arrival mismatches.

To evaluate the predictive ability of the two velocity models, we selected two unmodeled local events that were widely recorded by strong motion stations in the Seattle area, many of which were recently deployed. The first event, referred hereafter as the Carnation event, had a magnitude of 3.4 and occurred on May 25, 2010 at 47.679N, - 121.978W (28 km east of Seattle), at a depth of 6 km (Figure 9). This is a shallow crustal event with a hypocenter within the North American plate. The second event, referred hereafter as the Kingston event, had a magnitude of 4.5 and occurred on January 30, 2009 at 47.772N, 122.557W (25 km northwest of Seattle) at a depth of 58 km (Figure 10). This is a Benioff Zone event with a hypocenter located within the subducting Juan de Fuca plate. We used the finite-difference code of Liu and Archuleta (2002) to simulate these two earthquakes for comparison with the recorded data.

Since neither of the two local events have a hypocenter that is within our new model, we embedded our new model into the regional model of Stephenson (2007), which encompasses both hypocenter locations. We extracted the upper 3.5 km of our new model, and pasted it into the model of Stephenson (2007). We applied some averaging near the suture between the two models to avoid discontinuities, and then explicitly added a discontinuity to represent the Seattle fault. This fault discontinuity follows the frontal surface trace described by Blakely (2002), is dipping 45 degrees to the south, and is given a 10% velocity contrast that decays exponentially away from the fault surface.

Vertically propagating shear waves at periods above 3 seconds in a medium with velocities between 600-1500 m/s will not be strongly affected by a 3.5 km thick region, the maximum depth of our new velocity model within the regional velocity model. Body

and surface waves at periods between 1-2 seconds can be strongly affected by a 3.5 km thick region. We expect and observe that long period (>3 s) arrivals calculated using the two models to be very similar to one another in phase and amplitude, while shorter period waves are sometimes different.

The Carnation event was recorded on 27 stations located on stiff soil sites as shown in Figure 9a. For 15 of these stations, amplitudes for periods between 1-2 seconds calculated using our new model are closer to the data by more than 5% compared to amplitudes using the previous model. For 2 of these stations, there is less than 5% difference between the two models. For 10 stations, the previous model yields better amplitudes by more than 5%. We also averaged the misfit across all stations at different frequencies between 0.5-1 Hz (Figure 9b). We calculated the points on this figure by first dividing the synthetic amplitude by the data amplitude. Then we subtract one from the absolute value of the mean ratio for each station so that a value of zero indicates a perfect match in amplitude. Average amplitudes calculated using our new model are closer to the data than those calculated using the previous model at all frequencies in the range. Even though the previous model makes better predictions at some stations, the difference between the two models tends to be smaller at those stations than for stations where our new model does better, which is evident in the averages shown in Figure 9b.

In Figures 9c and 9d, we show a scatter plot of all of the amplitudes that are averaged to make Figure 9b. There is a significant amount of scatter that could represent either site effects from unconsolidated sediments or unmodeled structure. As a local crustal event, the seismic waves traveling from the hypocenter to each station travels ~ 20

km through heterogeneous upper crust. We will see that the Kingston event, a Benioff Zone earthquake, has a much tighter scatter plot due to smaller path effects.

In addition to the complications due to path effects there is some uncertainty in the moment magnitude for the Carnation event. The PNSN catalog states this event has an M_d of 3.4. Using a moment magnitude of 3.4 results in the amplitudes of the synthetics systematically overestimating the amplitudes of the data using both models. We found that simulating this event with a moment magnitude of 3.25 resulted in the best overall fit with the data. Amplitudes calculated with our new model are more closely clustered around the observed amplitudes, especially at longer periods in the range considered using this moment magnitude. In order to adjust the moment magnitude to best fit results from the previous model, the moment magnitude would have to be less than 3.25.

The Kingston event was recorded by 23 stations located on stiff soil sites as shown in Figure 10a. For 12 of these stations, amplitudes calculated using our new model are closer to the data by more than 5% compared to amplitudes using the previous model. For 8 of these stations, there is less than 5% difference between the two models. For 3 stations, the previous model yields better amplitudes by more than 5%. We also averaged the misfit across all stations at different frequencies between 0.5-1 Hz (Figure 10b). Between periods of 1.0-1.67 seconds our new model has amplitudes closer to the data, while the previous model has better amplitudes between 1.67-2.0 seconds. Compared to the Carnation event, synthetic amplitudes are closer to data amplitudes for both models, however our new model makes better predictions at most of the individual

stations. The scatter plots shown in Figures 10c and 10d show that amplitudes calculated using our new model are more clustered around the observed amplitudes.

Overall, improvement of our predictions over the predictions made with the previous model for the Kingston event is smaller than for the Carnation event. Since the Kingston event is almost directly below the Seattle Basin and at a depth of almost 60 km, most of the wave path is in the mantle with only the top 3.5 km different in the two models. For the Carnation event, which is a shallow crustal event, most of the wave path is in the crust and waves are traveling horizontally through our model for distances greater than 3.5 km. So, we our model will have a greater impact on the predictions made from shallow events.

INTERPRETATION

Due to the density of stations in the city of Seattle, we were able to resolve smaller features in the velocity structure than previous basin-wide models. As noted above, there is a pronounced low velocity zone just north of the Seattle Fault in Elliot Bay at the outlet of the Duwamish River, which is most evident, a 1 km depth. Basin sediments have lower velocities than the mostly crystalline rock to the south and north and we are able to resolve this contrast. To the west across Puget Sound, the fault trace shifts northward (Blakely *et al.*, 2002) which can be seen in our model at depths from 1-3 km. Our data do not cover the entire length of the Seattle fault, but in places where we have data coverage we observed the associated velocity contrast. Velocity variations within the basin reveal several sub-basins that could have at least two different origins. Deeper sub-basins are likely formed by the evolution of the basin through a combination of thrust and strike-slip tectonic motions while shallower sub-basins are likely the result of glacial action including uneven compaction, deposition, and erosion.

CONCLUSIONS

We use ambient noise to directly observe the shear wave velocity structure of the Seattle Basin. The 3D structure of deep crustal basins has a significant impact on the propagation of seismic waves and seismic hazards in the cities that sit atop them. Our shear wave model of the Seattle Basin contains more detail than the previous model used in seismic hazard assessments and may help explain some of the unmodeled amplitude scattering observed in previous efforts. We have shown quantitatively that our new model makes better predictions than the previous model for two local earthquakes.

Our method's strength is the resolving power of short period Rayleigh waves on shear wave velocity in the upper few kilometers without the need to precisely know Poisson's ratio. Our method's weaknesses are the inability to precisely resolve sharp discontinuities and uniquely constrain velocities in the top 250 m. Resolving sharp discontinuities is better suited to reflection seismology and determining amplification factors due to shallow, unconsolidated sediment is better suited to observations of strong motions and more local or point measurements of sediment thicknesses and shear wave velocity. We believe that our new model can be applied to predict levels of ground shaking with greater accuracy than the current seismic hazard maps for Seattle, as demonstrated by the two events we examined, due to more accurate modeling of shear wave velocities in the upper 3-4 km of the basin. We believe that most of the remaining misfit is likely due to site effects, sharp discontinuities not resolved by the tomography, and unmodeled structure from outside of our data coverage.

Further improvements in the Seattle Basin velocity model could be achieved using a more optimal station arrangement, more broadband instruments, a longer

recording duration, and developing a joint inversion that explicitly includes geological information about sharp discontinuities such as faults and basin edges. However, using a limited, legacy dataset we were able to make measurable improvements to amplitude predictions for two local earthquakes at frequencies relevant to seismic hazard assessments.

DATA AND RESOURCES

This study uses data collected during the SHIPS 2002 experiment, which was obtained from the IRIS Data Management Center. This study also uses data collected by Earthscope's Transportable Array (TA) and the Pacific Northwest Seismic Network (PNSN), also available from the IRIS Data Management Center.

ACKNOWLEDGEMENTS

The authors wish to acknowledge Tom Pratt for his assistance in analyzing the SHIPS 2002 dataset and Art Frankel for consultations regarding the Seattle Basin.

REFERENCES

- Atwater, B. F. (1992), Geologic evidence for earthquakes during the past 2000 years along the Copalis River, southern coastal Washington, *J Geophys Res* **97** 1901-1919.
- Barberopoulou, A., A. Qamar, T. L. Pratt, K. C. Creager, and W. P. Steele (2004), Local amplification of seismic waves from the Denali earthquake and damaging seiches in Lake Union, Seattle, Washington, *Geophys. Res. Lett.* **31** 5.
- Bensen, G. D., M. H. Ritzwoller, M. P. Barmin, A. L. Levshin, F. Lin, M. P. Moschetti, N. M. Shapiro, and Y. Yang (2007), Processing seismic ambient noise data to obtain reliable broad-band surface wave dispersion measurements, *Geophys J Int* **169** 1239-1260.
- Blakely, R. J., R. E. Wells, C. S. Weaver, and S. Y. Johnson (2002), Location, structure, and seismicity of the Seattle fault zone, Washington; evidence from aeromagnetic anomalies, geologic mapping, and seismic-reflection data, *Bull. Geol. Soc. Am.* **114** 169-177.
- Booth, D. B. (1994), Glaciofluvial infilling and scour of the Puget Lowland, Washington, during ice-sheet glaciation, *Geology* **22** 695-698.
- Brocher, T. M., T. E. Parsons, R. J. Blakely, N. I. Christensen, M. A. Fisher, R. E. Wells, U. S. ten Brink, T. L. Pratt, R. S. Crosson, K. C. Creager, N. P. Symons, L. A. Preston, T. Van Wagoner, K. C. Miller, C. M. Snelson, A. M. Trehu, V. E. Langenheim, G. D. Spence, K. Ramachandran, R. D. Hyndman, D. C. Mosher, B. C. Zelt, and C. S. Weaver (2001), Upper crustal structure in Puget Lowland, Washington; results from the 1998 seismic hazards investigation in Puget Sound, *J Geophys Res* **106** 13.
- Brocher, T. M., R. J. Blakely, and R. E. Wells (2004), Interpretation of the Seattle uplift, Washington as a passive roof duplex, *Bull. Seism. Soc. Am.* **94** 1379-1401.
- Brocher, T. M. (2005), Empirical relations between elastic wavespeeds and density in the Earth's crust, *Bull. Seism. Soc. Am.* **95** 2081-2092.
- Frankel, A. D., D. L. Carver, E. Cranswick, M. E. Meremonte, T. Bice, and D. E. Overturf (1999), Site response for Seattle and source parameters of earthquakes in the Puget Sound region, *Bull. Seism. Soc. Am.* **89** 468-483.
- Frankel, A. D., D. L. Carver, and R. A. Williams (2002), Nonlinear and linear site response and basin effects in Seattle for the M 6.8 Nisqually, Washington, earthquake, *Bull. Seism. Soc. Am.* **92** 2090-2109.

- Frankel, A. D., W. J. Stephenson, D. L. Carver, R. A. Williams, J. K. Odum, and S. Rhea (2007), Seismic hazard maps for Seattle, Washington, incorporating 3D sedimentary basin effects, nonlinear site response, and rupture directivity, *U.S. Geological Survey Open-File Report 2007-1175*.
- Frankel, A. D., W. J. Stephenson, and D. Carver (2009), Sedimentary Basin Effects in Seattle, Washington: Ground-Motion Observations and 3D Simulations, *Bull. Geol. Soc. Am.* **99** 1579-1611.
- Goldfinger, C., C. H. Nelson, and J. E. Johnson (2003), Deep-water turbidites as Holocene earthquake proxies: the Cascadia subduction zone and Northern San Andreas Fault systems, *Ann Geophys* **46** 1169-1194.
- Hartzell, S., D. Carver, E. Cranswick, and A. D. Frankel (2000), Variability of site response in seattle, Washington, *Bull. Seism. Soc. Am.* **90** 1237-1250.
- Haugerud, R. A., D. J. Harding, S. Y. Johnson, J. L. Harless, C. S. Weaver, and B. L. Sherrod (2003), High-resolution lidar topography of the Puget Lowland, Washington, *GSA Today* **13** 4-10.
- Johnson, S. Y., C. J. Potter, J. M. Armentrout, J. J. Miller, C. A. Finn, and C. S. Weaver (1996), The southern Whidbey Island Fault; an active structure in the Puget Lowland, Washington, *Bull. Geol. Soc. Am.* **108** 334-354.
- Lees, J. M., and R. S. Crosson (1990), Tomographic Imaging of Local Earthquake Delay Times for 3-Dimensional Velocity Variation in Western Washington, *J Geophys Res* **95** 4763-4776.
- Li, Q., W. S. D. Wilcock, T. L. Pratt, C. M. Snelson, and T. M. Brocher (2006), Seismic attenuation structure of the Seattle basin, Washington State, from explosive-source refraction data, *Bull. Seism. Soc. Am.* **96** 553-571.
- Liu, P. C., and R. J. Archuleta (2002), The effect of a low-velocity surface layer on simulated ground motion, *Seismol Res Lett* **73** 267.
- Pitarka, A., R. Graves, and P. Somerville (2004), Validation of a 3D Model of the Puget Sound Region Based on Modeling Ground Motion from the 28 February 2001 Nisqually Earthquake, *Bull. Geol. Soc. Am.* **94** 1670-1689.
- Pratt, T. L., S. Y. Johnson, C. J. Potter, W. J. Stephenson, and C. A. Finn (1997), Seismic reflection images beneath Puget Sound, western Washington State; the Puget Lowland thrust sheet hypothesis, *J Geophys Res* **102** 27,469-427,489.

- Pratt, T. L., T. M. Brocher, C. S. Weaver, K. C. Creager, C. M. Snelson, R. S. Crosson, K. C. Miller, and A. M. Trehu (2003a), Amplification of seismic waves by the Seattle Basin, Washington State, *Bull. Seism. Soc. Am.* **93** 533-545.
- Pratt, T. L., K. L. Meagher, T. M. Brocher, T. Yelin, R. D. Norris, L. Hultgrien, E. A. Barnett, and C. S. Weaver (2003b), Earthquake recordings from the 2002 Seattle Seismic Hazard Investigation of Puget Sound (SHIPS), Washington State, *Open File Rep U S Geol Surv* 72.
- Ramachandran, K., S. E. Dosso, C. A. Zelt, G. D. Spence, R. D. Hyndman, and T. M. Brocher (2004), Upper crustal structure of southwestern British Columbia from the 1998 Seismic Hazards Investigation in Puget Sound, *J Geophys Res* **109** B09303.
- Ramachandran, K., S. E. Dosso, G. D. Spence, R. D. Hyndman, and T. M. Brocher (2005), Forearc structure beneath southwestern British Columbia: A 3-D tomography velocity model, *J Geophys Res* **110** B02303.
- Ramachandran, K., R. D. Hyndman, and T. M. Brocher (2006), Regional P-wave velocity structure of the Northern Cascadia subduction zone, *J Geophys Res* **111** B12301.
- Riddihough, R. P. (1984), Recent movements of the Juan de Fuca plate system, *J Geophys Res* **89** 6980-6994.
- Satake, K., K. Wang, and B. F. Atwater (2003), Fault slip and seismic moment of the 1700 Cascadia earthquake inferred from Japanese tsunami descriptions, *J Geophys Res* **108** 17.
- Schultz, A. P., and R. S. Crosson (1996), Seismic velocity structure across the central Washington Cascade Range from refraction interpretation with earthquake sources, *J Geophys Res* **101** 27,899-827,915.
- Sherrod, B. L., T. M. Brocher, C. S. Weaver, R. C. Bucknam, R. J. Blakely, H. M. Kelsey, A. R. Nelson, and R. Haugerud (2004), Holocene fault scarps near Tacoma, Washington, USA, *Geology* **32** 9-12.
- Snelson, C. M., T. M. Brocher, K. C. Miller, T. L. Pratt, and A. M. Trehu (2007), Seismic Amplification within the Seattle Basin, Washington State: Insights from SHIPS Seismic Tomography Experiments, *Bull. Seism. Soc. Am.* **97** 1432-1448.
- Stephenson, W. J. (2007), Velocity and density models incorporating the Cascadia Subduction Zone for 3D earthquake ground motion simulation, *Open File Rep U S Geol Surv* **2007-1348**.
- Symons, N. P., and R. S. Crosson (1997), Seismic velocity structure of the Puget Sound region from 3-D non-linear tomography, *Geophys. Res. Lett.* **24** 2593-2596.

- Takeuchi, H., and M. Saito (1972), Seismic Surface Waves, in *Methods in Computational Physics*, edited, pp. 217-195.
- ten Brink, U. S., P. C. Molzer, M. A. Fisher, R. J. Blakely, R. C. Bucknam, T. Parsons, R. S. Crosson, and K. C. Creager (2002), Subsurface geometry and evolution of the Seattle fault zone and the Seattle Basin, Washington, *Bull. Seism. Soc. Am.* **92** 1737-1753.
- ten Brink, U. S., J. Song, and R. C. Bucknam (2006), Rupture models for the A.D. 900-930 Seattle Fault earthquake from uplifted shorelines, *Geology* **34** 585-588.
- Van Wagoner, T. M., R. S. Crosson, K. C. Creager, G. F. Medema, L. A. Preston, N. P. Symons, and T. M. Brocher (2002), Crustal structure and relocated earthquakes in the Puget Lowland, Washington, from high-resolution seismic tomography, *J Geophys Res* **107** 23.
- Wells, R. E., C. S. Weaver, and R. J. Blakely (1998), Fore-arc migration in Cascadia and its neotectonic significance, *Geology* **26** 759-762.
- Wells, R. E., and R. W. Simpson (2001), Northward migration of the Cascadia forearc in the northwestern U. S. and implications for subduction deformation, *Earth Planets Space* **53** 275-283.

Andrew A. Delorey (Corresponding Author)

John E. Vidale

Department of Earth and Space Sciences

University of Washington

Johnson Hall Rm-070, Box 351310

4000 15th Avenue NE

Seattle, WA 98195-1310

Figure 1. Geometry of basins as revealed by gravity variations around Seattle, Everett, and Tacoma, Washington (Brocher *et al.*, 2001).

Figure 2. Stations used for this study. The closed curve indicates the approximate boundary to the Seattle Basin based on the gravity measurements of Brocher *et al.*, (2001). The gray patches indicate the Seattle fault, Tacoma fault, and South Whidbey Island fault. The circles indicate broadband stations of the PNSN, triangles indicate broadband stations of the Earthscope's TA, and stars indicate stations of the SHIPS 2002 array.

Figure 3. Two examples of empirical Green's functions bandpass filtered between 1-10 seconds period. The two paths shown on the station map at top are labeled (a) and (b) and correspond with the bandpassed waveforms shown below.

Figure 4. At left is the inversion result and at right is the synthetic model used to test the resolution of our dataset.

Figure 5. Lines represent paths for Rayleigh Waves used to image the Seattle Basin. The period is indicated at the lower right of each subfigure. Triangles represent stations of the SHIPS array.

Figure 6. Rayleigh wave phase velocities for periods between 2 and 10 seconds. Black triangles represent stations of the SHIPS 2002 array. The upper gray patch

indicates the location of the South Whidbey Island fault. The lower gray patch indicates the location of the Seattle Fault zone. The closed curve indicates the approximate boundary to the Seattle Basin based on the gravity measurements of Brocher *et al.*, (2001).

Figure 7. Our shear wave velocity model (a) and the model of Stephenson (2007) (b).

Depths are indicated on each row. The upper gray patch indicates the location of the South Whidbey Island fault. The lower gray patch indicates the location of the Seattle Fault zone. The closed curve indicates the approximate boundary to the Seattle Basin based the gravity measurements of Brocher *et al.*, (2001). The six-sided polygon represents the region of the model that is covered by our dataset.

Figure 8. Velocity data and synthetics of station QCOR for the Carnation event. Data are shown in black and synthetics are shown in gray. The shear, Love, and Rayleigh wave arrivals are denoted with “S”, “L”, and “R”, respectively. Traces are bandpass filtered with corner frequencies of 0.5-1 Hz.

Figure 9. Carnation event. (a) The asterisk indicates the event epicenter. Outlined station names indicate stations where our new model produces better PGVs than the previous model. Bold station names indicate stations where the previous model produces better PGVs than our new model. Italicized station names indicate stations where PGVs produced by the two models are within 5%. (b)

Shown is the average misfit as a function of frequency. Solid squares indicate PGV misfit for the previous model and open squares indicate PGV misfit for our new model. Scatter plot for PGVs for all stations and all frequencies shown in (a) and (b) calculated from our new model (c) and the previous model (d) compared to the observed amplitudes, in four bins between 0.5-1 Hz, are shown from left to right then top to bottom. In these four axes, when a square is on the centerline with a slope of one, that indicates a perfect match of PGVs between data and synthetic. The next line with a smaller slope indicates that the synthetic is 25% greater than the data. The next two lines with smaller slopes indicate 50% and 100% greater, respectively. The lines with a slope greater than one indicate 1/1.25, 1/1.5, and 1/2, respectively, with the data greater than the synthetic. The black curve, only partially shown indicates the approximate boundary to the Seattle Basin based on the gravity measurements of Brocher *et al.*, (2001) and the gray patch indicates the location of the Seattle Fault zone.

Figure 10. Kingston event. (a) The asterisk indicates the event epicenter. Outlined station names indicate stations where our new model produces better PGVs than the previous model. Bold station names indicate stations where the previous model produces better PGVs than our new model. Italicized station names indicate stations where PGVs produced by the two models are within 5%. (b) Shown is the average misfit as a function of frequency. Solid squares indicate PGV misfit for the previous model and open squares indicate PGV misfit for our new model. Scatter plot for PGVs for all stations and all frequencies shown in (a)

and (b) calculated from our new model (c) and the previous model (d) compared to the observed amplitudes, in four bins between 0.5-1 Hz, are shown from left to right then top to bottom. In these four axes, when a square is on the centerline with a slope of one, that indicates a perfect match of PGVs between data and synthetic. The next line with a smaller slope indicates that the synthetic is 25% greater than the data. The next two lines with smaller slopes indicate 50% and 100% greater, respectively. The lines with a slope greater than one indicate 1/1.25, 1/1.5, and 1/2, respectively, with the data greater than the synthetic. The black curve, only partially shown indicates the approximate boundary to the Seattle Basin based on the gravity measurements of Brocher *et al.*, (2001) and the gray patch indicates the location of the Seattle Fault zone.

Figure S1. Shown are west to east vertical cross-sections of our shear wave velocity model. North and west-east distances correspond an origin in the lower left corner in Figure 7a.

Figure S2. Shown are south to north vertical cross-sections of our shear wave velocity model. East and south-north distances correspond to an origin in the lower left corner in Figure 7a.

Figure S3. Contours from the shear wave model of Snelson *et al.*, (2007) (gray) and the same region in our model (black). This figure shows a total of 4 km in depth.

The top contour, below the horizontal surface boundary, from each model is 1 km/s and the contour interval is 0.25 km/s. The locations of Puget Sound and Lake Washington are indicated above.

Figure 1

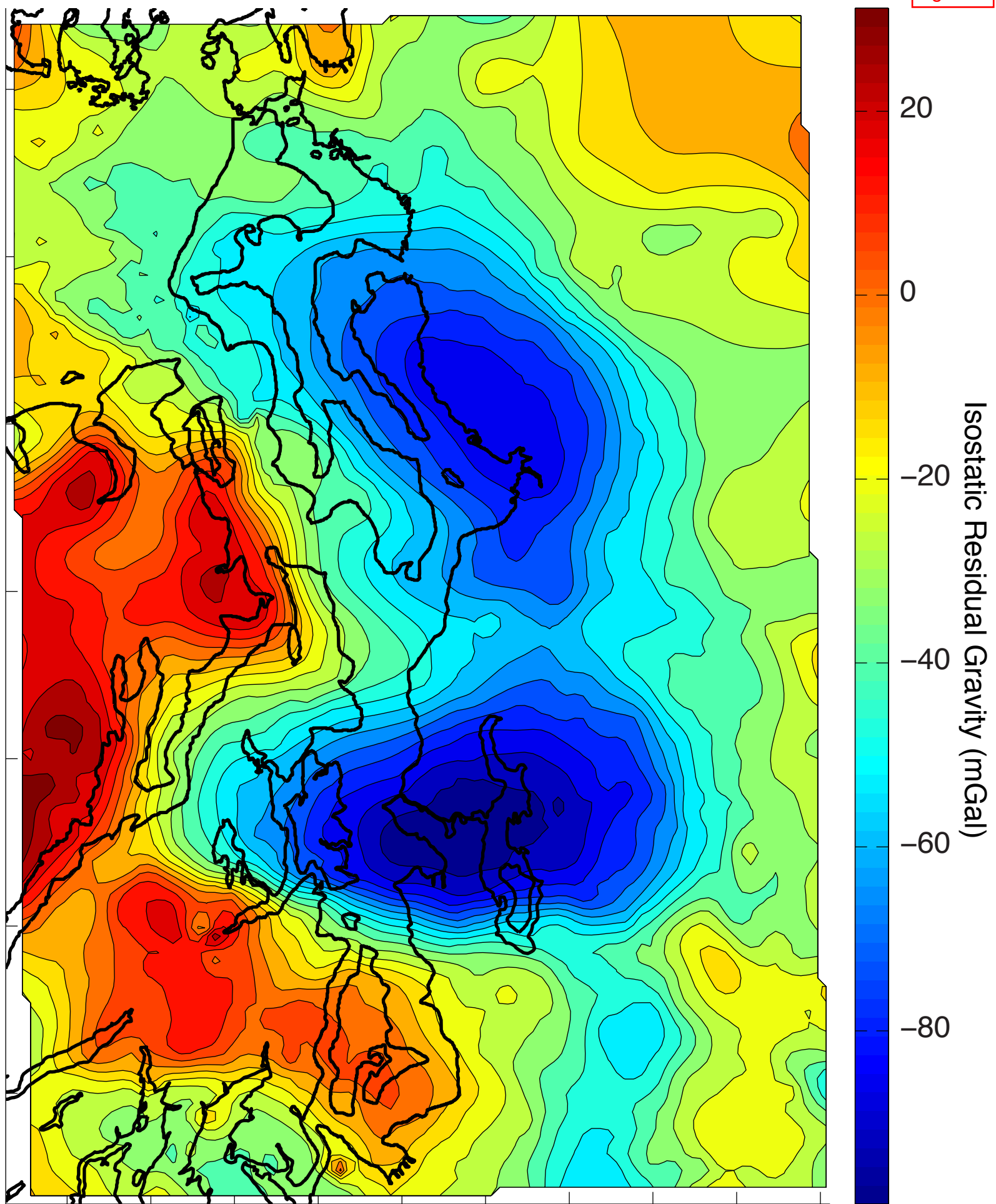
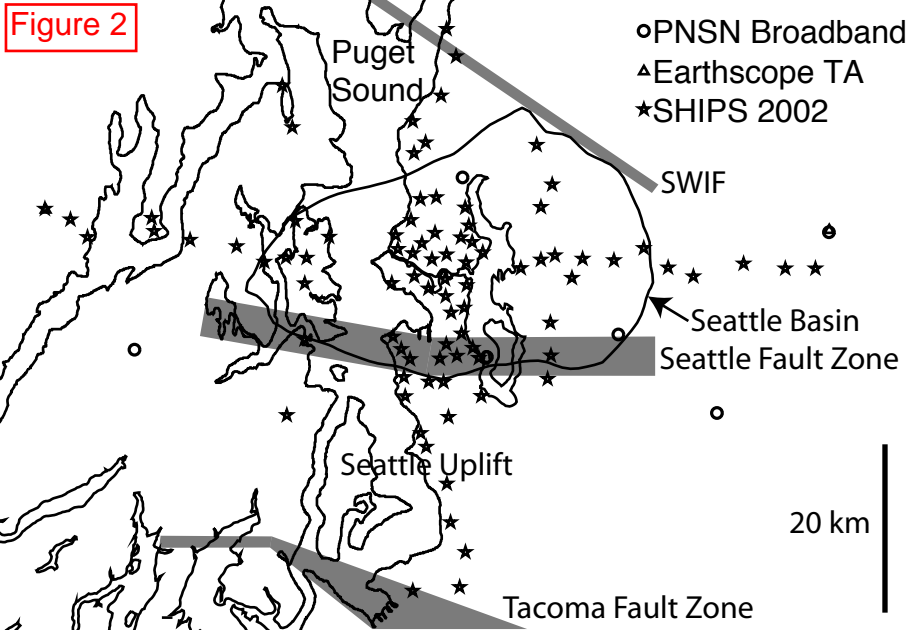


Figure 2



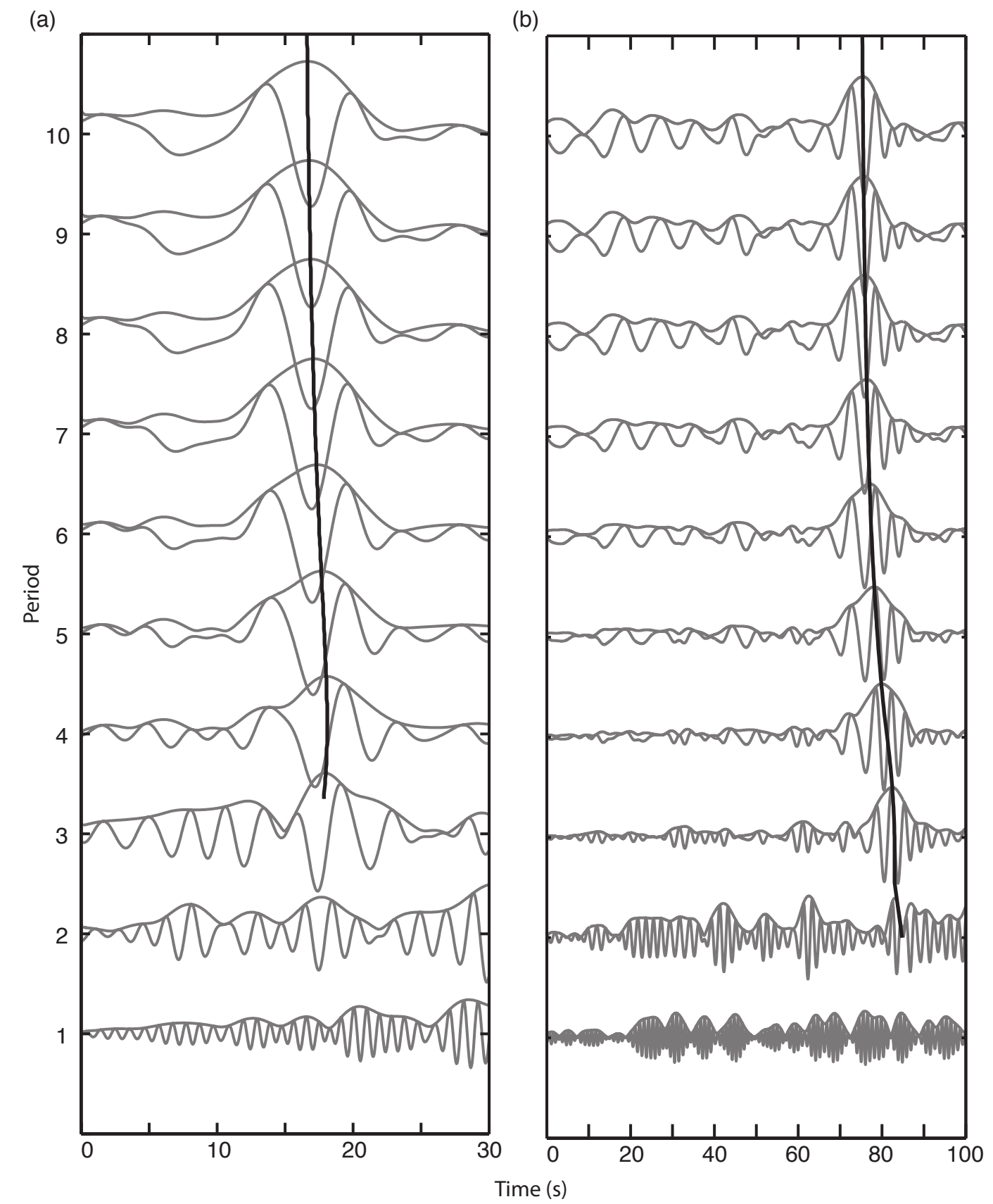
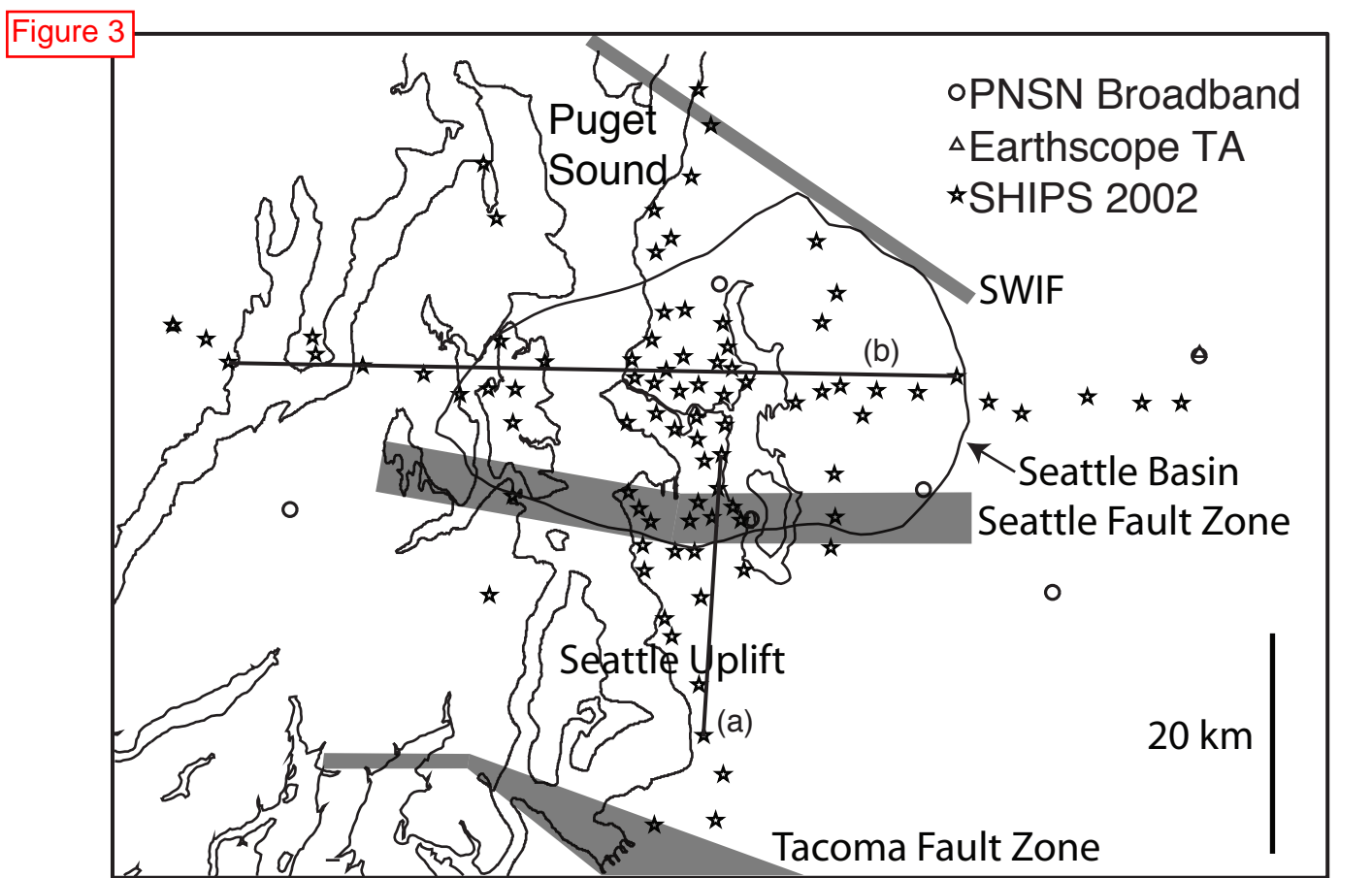
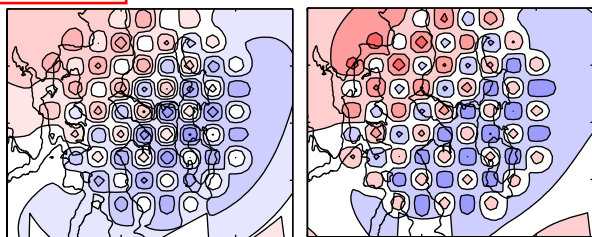
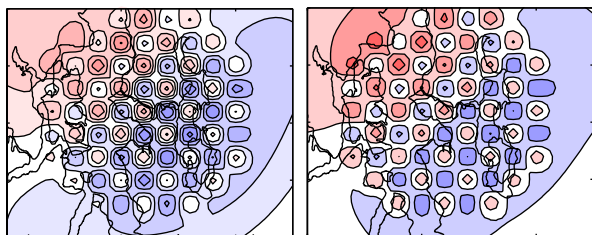


Figure 4

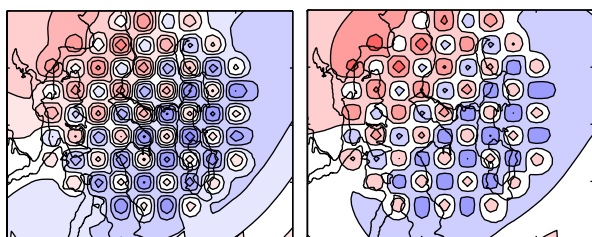
Period = 10s



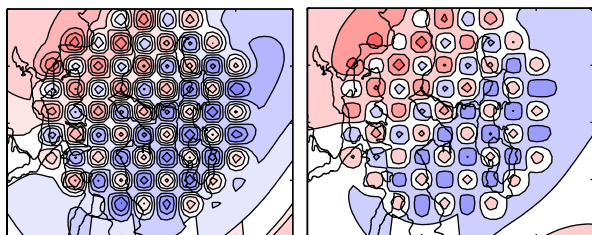
Period = 8s



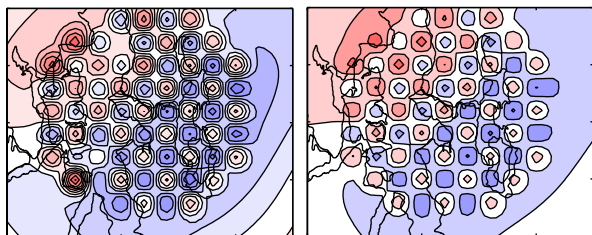
Period = 6s



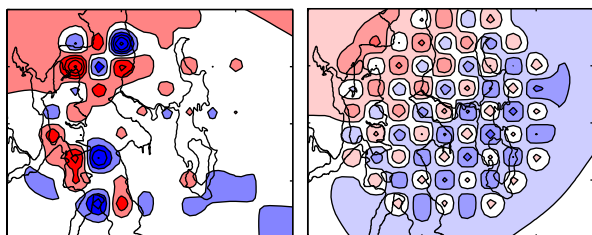
Period = 4s



Period = 3s



Period = 2s



10 km

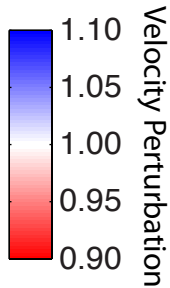


Figure 5

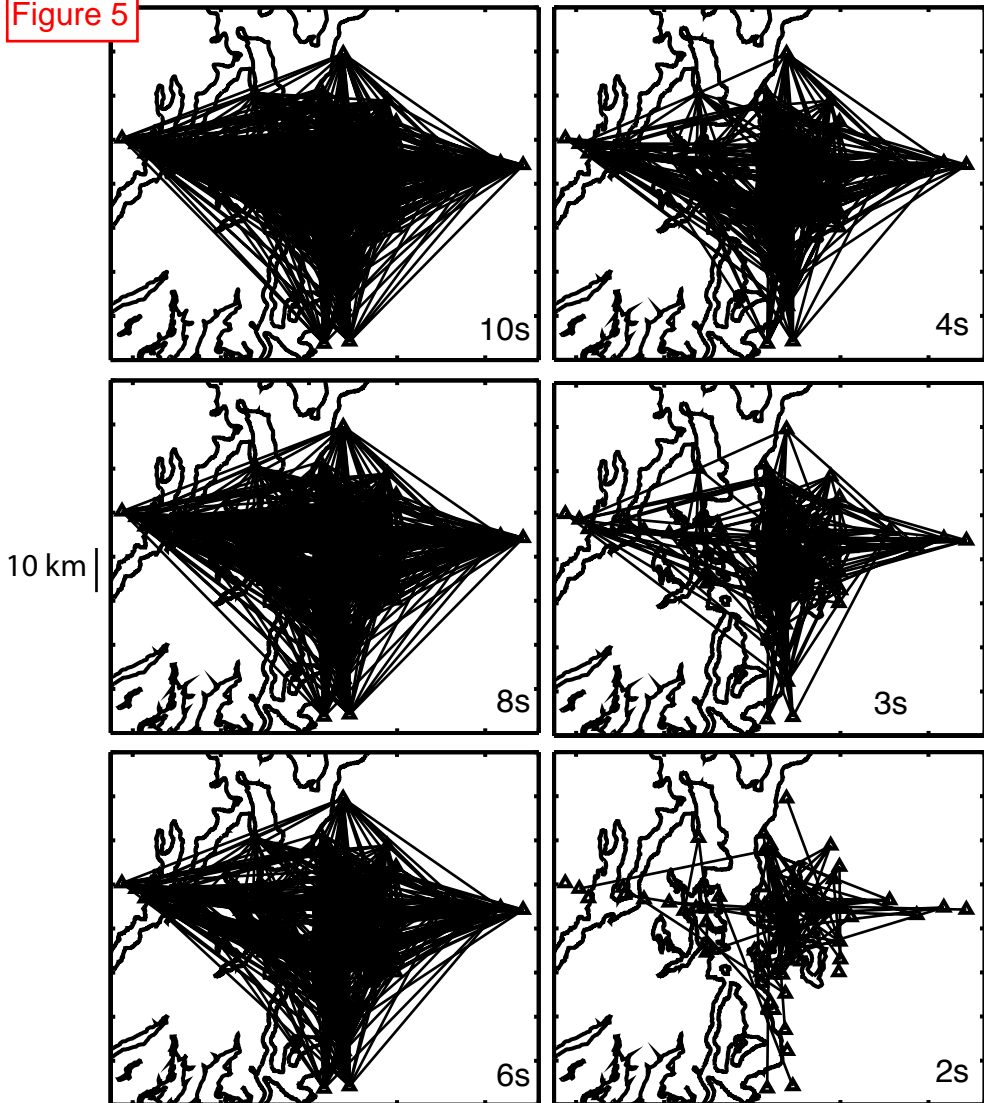


Figure 6

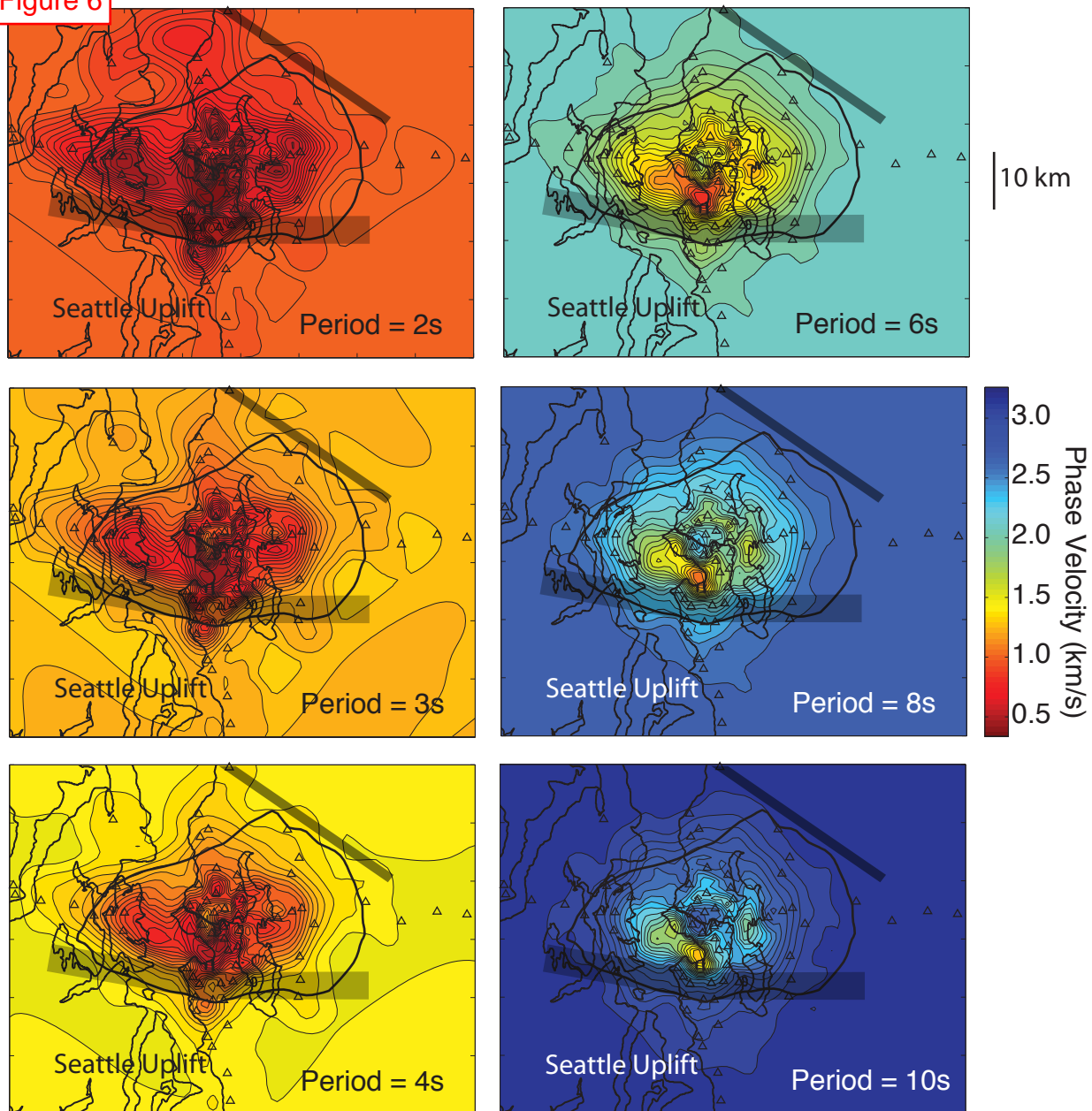


Figure 7

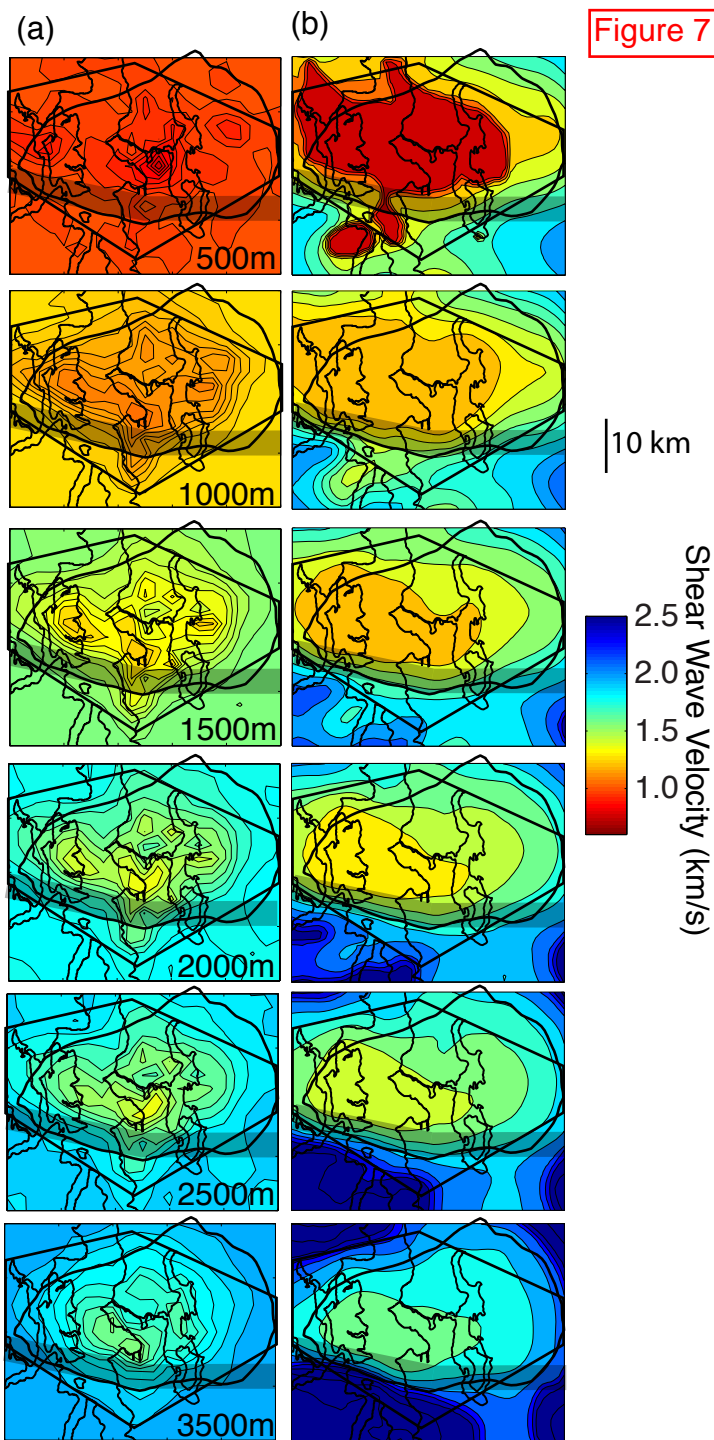
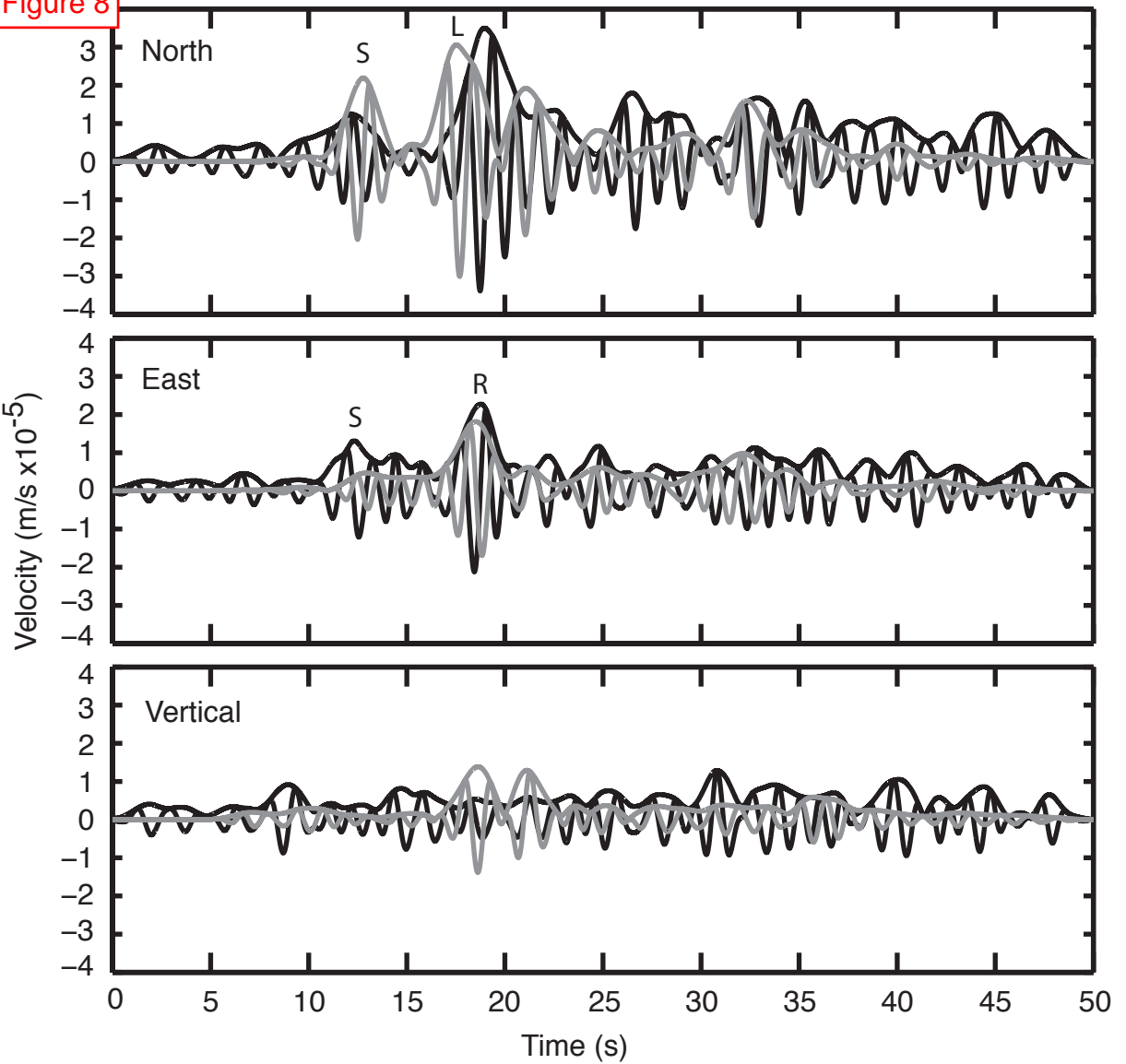
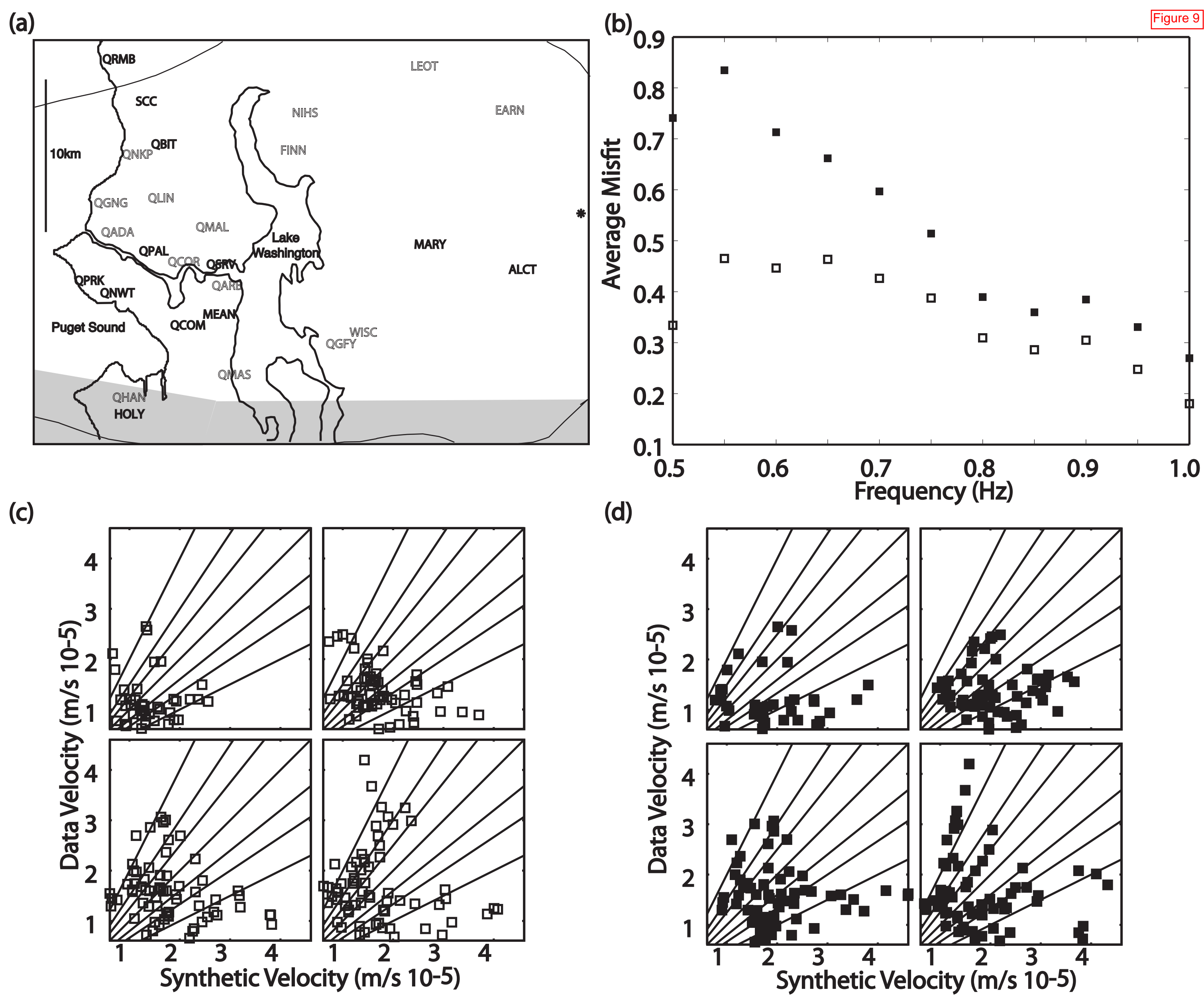
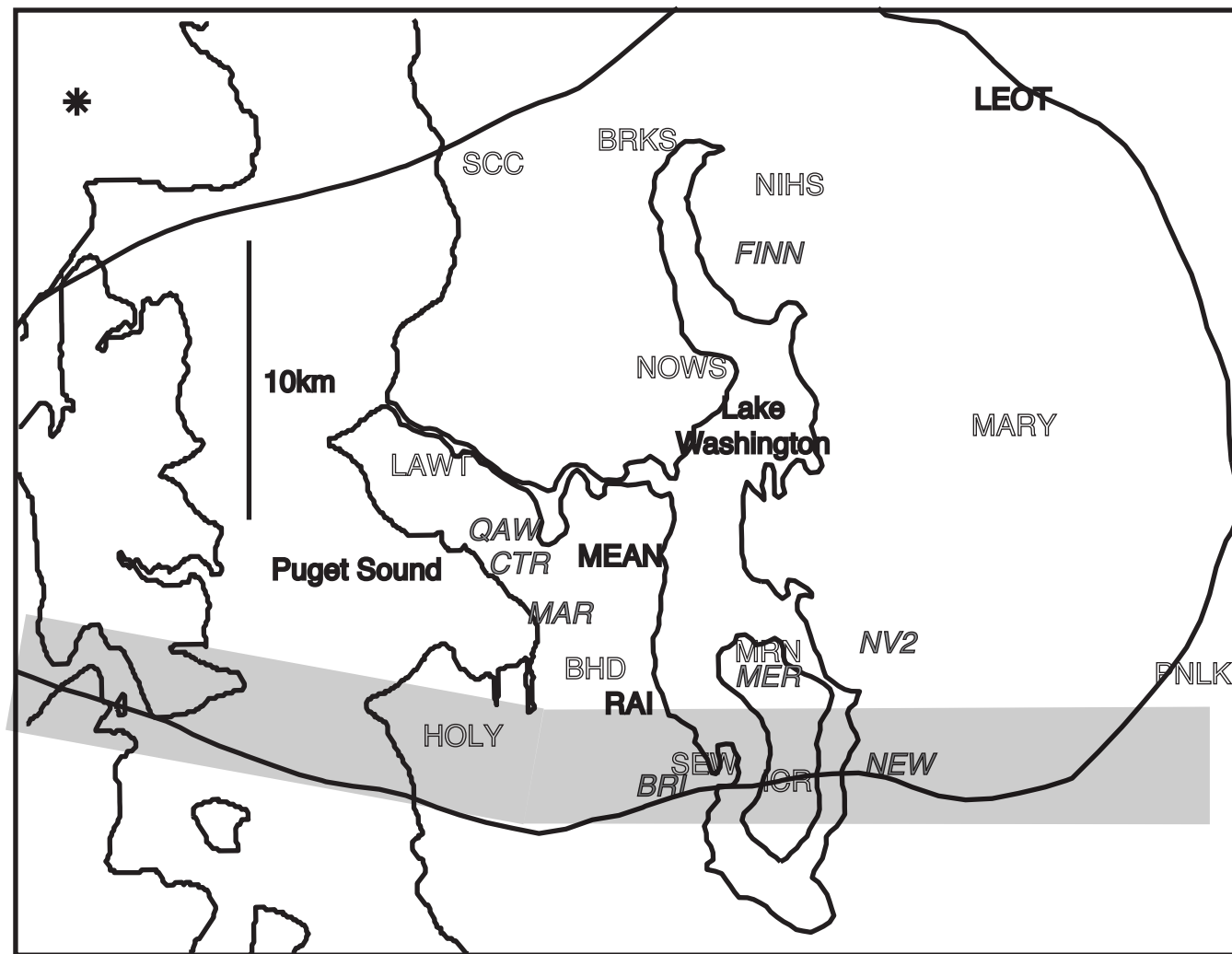


Figure 8

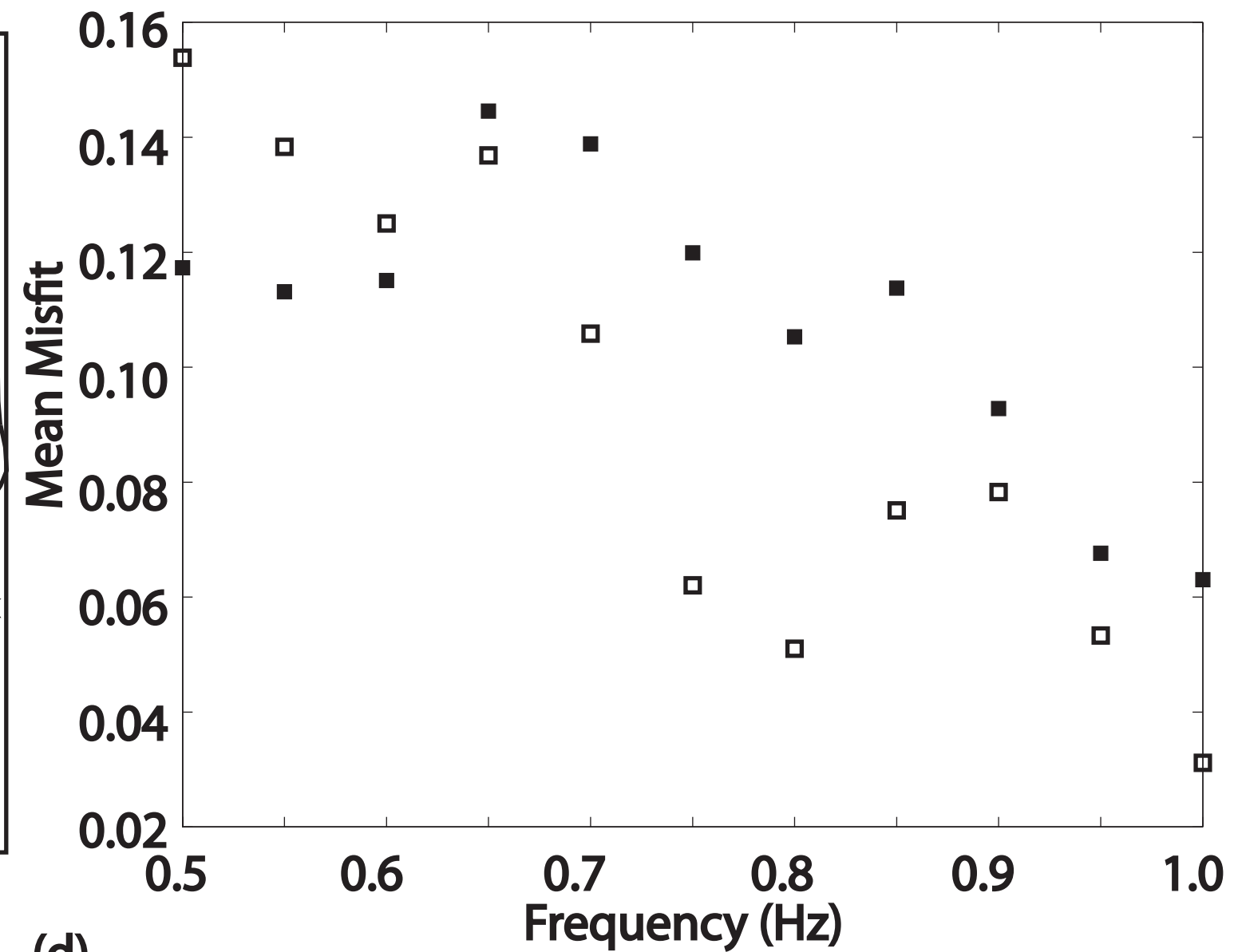




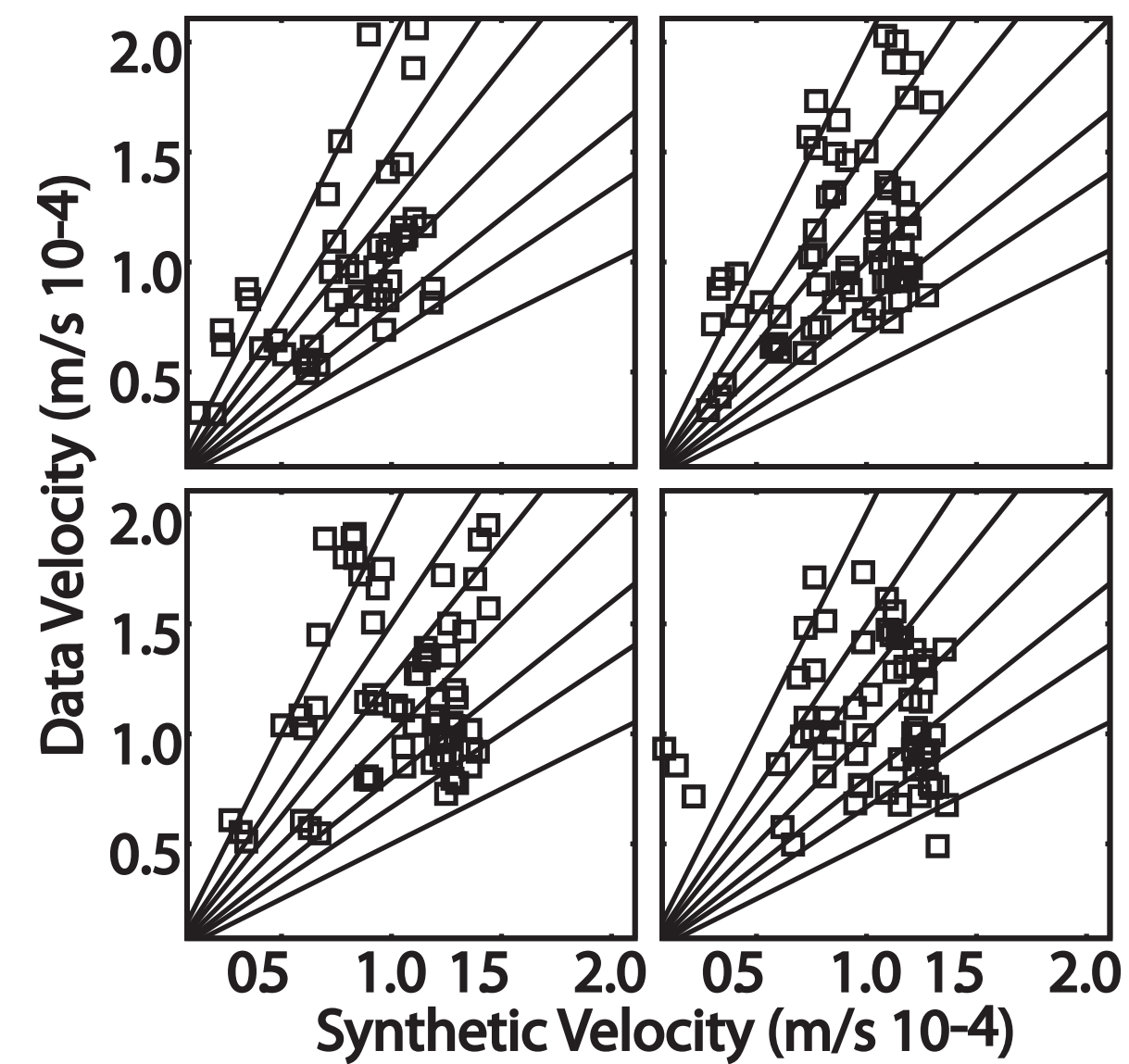
(a)



(b)



(c)



(d)

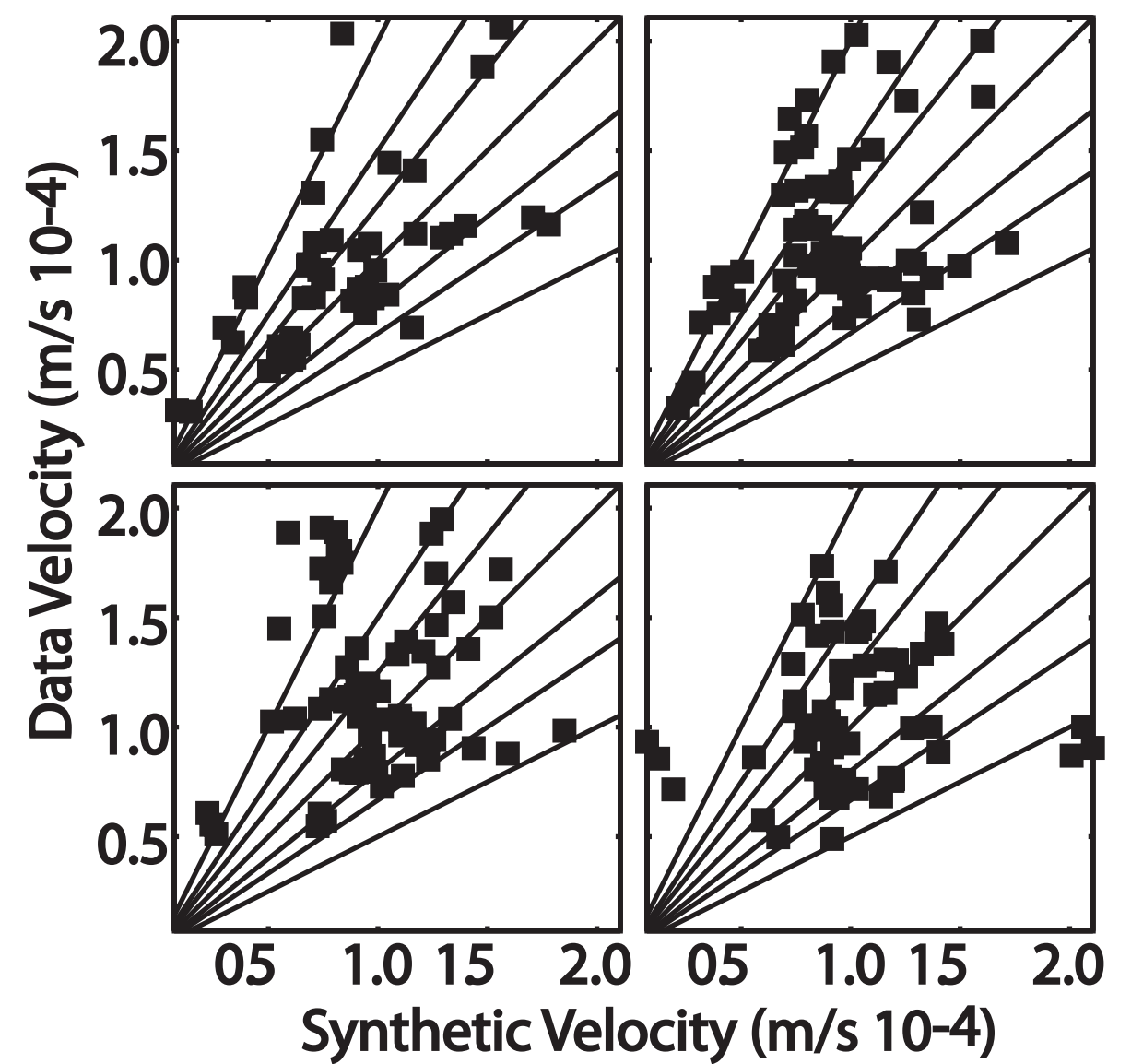


Figure S1

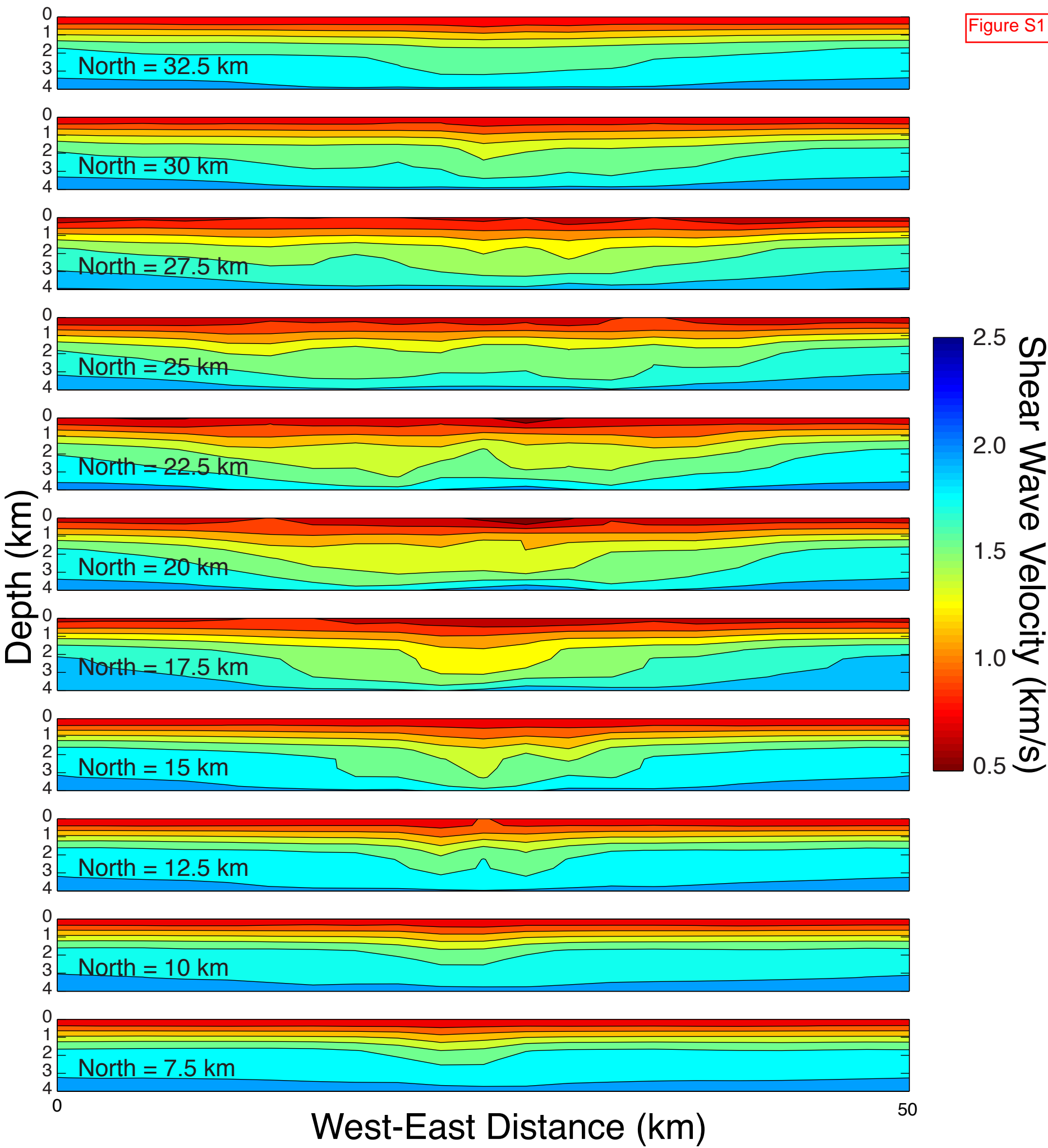


Figure S2

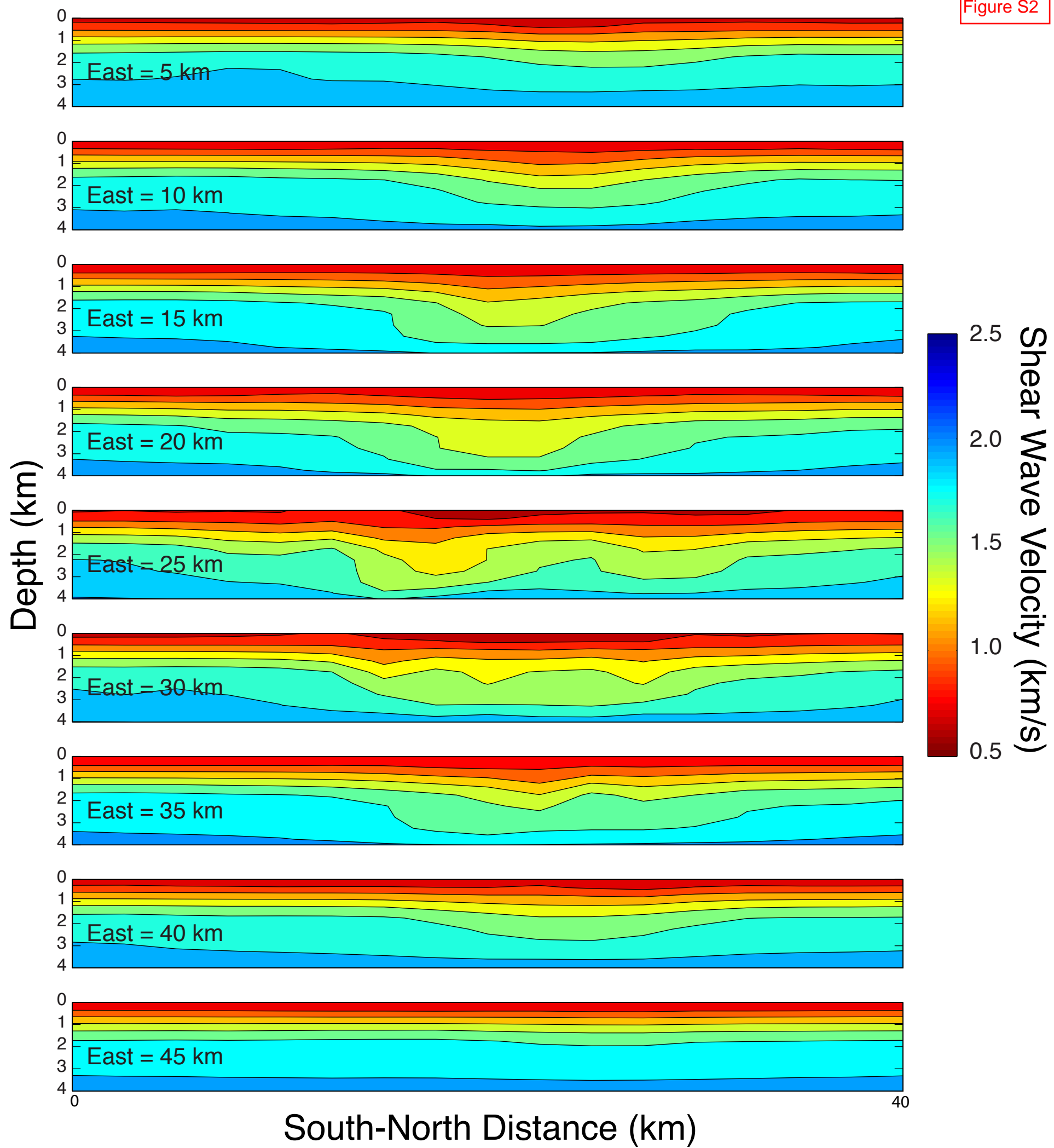


Figure S3

